VALIDATION OF A SURROGATE-BASED METHODOLOGY FOR LOW-NOISE UAV/UAM ROTOR DESIGN

Adam Sieradzki*, Lukasiewicz Research Network, Institute of Aviation, Warsaw, Poland
Pawel Kekus*, Lukasiewicz Research Network, Institute of Aviation, Warsaw, Poland
Witold Klimczyk*, Lukasiewicz Research Network, Institute of Aviation, Warsaw, Poland

Abstract

One of the main problems of the Unmanned Aerial Vehicles (UAV) and Urban Air Mobility (UAM) markets is the noise generated by these aircraft. The work focuses on the development of a design methodology for low-noise, high-efficiency propellers. The method's capabilities were demonstrated and validated through multi-objective UAV propeller optimization, the manufacture of technology demonstrators, and tests on a dedicated test stand within an anechoic chamber. The developed acoustic facility proved capable of providing high-quality propeller acoustic and performance measurements required for validation purposes. The proposed surrogate-based optimization framework allowed to find a set of non-dominated solutions improved relative to the benchmark baseline, both in terms of aerodynamic performance and noise level. The observed optimization direction and the characteristics of the resultant geometries align with the expectations and trends outlined in the existing literature. The conducted experimental studies allowed to verify the predicted improvements, revealing the challenges tied to the numerical prediction of low-Reynolds number propeller performance and the necessity of minimizing undesirable noise sources in experimental studies.

1. NOTATION

Symbols:

c	Chord length, m
C_T	Thrust coefficient, $T/(\rho_\infty \pi \Omega^2 R^4)$
C_Q	Torque coefficient, $Q/(\rho_\infty \pi \Omega^2 R^5)$
F_{ax} / F_{tan}	Axial/tangential force, N
FM	Figure of Merit, $C_T^{1.5}/\left(C_Q\sqrt{2}\right)$
R	Rotor radius, m
T	Thrust, N
Q	Torque, Nm
β	Blade twist angle, deg
ρ_∞	Freestream density, kg/m³
Ω, ω	Propeller speed of rotation, rad/s

Acronyms:

BET	Blade Element Theory
BPF	Blade Passing Frequency
CAA	Computational Aeroacoustics
CAD	Computer-Aided Design
CFD	Computational Fluid Dynamics
OASPL	Overall Sound Pressure Level
RANS	Reynolds-Averaged Navier-Stokes
RPM	Revolutions Per Minute
SBO	Surrogate-Based Optimization
SPL	Sound Pressure Level
UAM	Urban Air Mobility
UAV	Unmanned Aerial Vehicle

2. INTRODUCTION

The increasing diversity and popularity of Unmanned Aerial Vehicles (UAVs) and Urban Air Mobility (UAM) vehicles have led to a closer examination of their safety and environmental impact (Ref. 1). Concurrently, there is a growing awareness of the negative effects of noise on human health and well-being (Ref. 2), which has prompted stricter noise-related regulations. This has consequently put more pressure on manufacturers to minimize the noise produced by their products. In the case of unmanned air systems, the main source of noise is typically the propulsion system, with propellers being the primary

*All authors have contributed equally.

contributors to the bothersome tones emitted (Ref. 3).

The development of the methodology for designing low-noise rotors is a step ahead of the introduction of regulations regarding the acceptable level of noise emitted by UAVs/UAMs. Rotor noise reduction technology is still not sufficiently developed, but it is necessary to enable the growth of the UAV/UAM industry on a large scale. Current noise mitigation solutions often result in unacceptable performance degradation.

A wide range of computational methods are now available to evaluate the performance and noise generated by propellers. Because of their cost-effectiveness and suitability during the initial design phases, conventional and inexpensive methods like those based on the Blade Element Theory (BET) are widely utilized for the design and optimization of propeller aerodynamics (Ref. 4). When paired with compact monopole/dipole formulations like the Ffowcs-Williams and Hawkings (FWH) method for noise computation, these approaches offer reasonable predictions for tonal noise and can facilitate the creation of quieter propellers (Ref. 5–7). Their limitations stem from the simplicity of the techniques employed. Particularly in scenarios involving low Reynolds numbers flows, it becomes important to consider the contribution of broadband noise, as its intensity might match that of the tonal component (Ref. 8). For calculating the broadband noise originating from the turbulent boundary layer interaction with the trailing edge of the blade, low fidelity semi-empirical wall-pressure spectrum models can be employed (Ref. 9).

Advanced techniques for Computational Aeroacoustics (CAA) involve using a high-resolution Computational Fluid Dynamics (CFD) model, such as Large Eddy Simulation (LES), hybrid Reynolds-Averaged Navier-Stokes (RANS) and LES, wall-modeled LES (Ref. 10), or the Lattice-Boltzmann Method (Ref. 11). Nevertheless, these inherently unsteady methods cannot be practically incorporated into optimization processes due to their computationally expensive nature.

While the utilization of low-fidelity methods is established in the realm of propeller design and optimization, transitioning to higher-fidelity methods presents a logical progression for achieving more effective outcomes. Adjoint methods (Ref. 12) and global Surrogate-Based Optimization (SBO) frameworks (Ref. 13) have been employed in optimization processes based on RANS simulations. Blade-resolved CFD methods allow for a detailed analysis of the aerodynamics of a generic propeller, taking into consideration various global and local geometric features that are often not adequately captured by low-fidelity methods. As a result, the geometry parametrization based on Computer-Aided Design (CAD) software can be employed for optimization, eliminating the need for reliance on tip-loss models or other sources of error inherent in low-fidelity methods.

In the current work, a methodology for designing rotors with low noise emission and high performance is described and validated. The proposed methodology is based on blade geometry-resolved CFD, which is considered to allow for accurate modeling of a rotor in hover without assumptions regarding its geometry and performance. Finally, SBO is used to obtain optimal aeroacoustic solutions at an affordable computational cost and time.

The capabilities of the method are demonstrated on the UAV scale, by performing optimization on a 30 cm diameter propeller, manufacturing technology demonstrators, and testing on a dedicated test stand in a newly built anechoic chamber. Such a comprehensive approach was chosen to allow for reliable validation of the computational tools and optimization results and to ensure the high credibility of the study.

3. METHODOLOGY

Building the rotor design methodology required several issues to be taken into account, e.g. parameterization of blade geometry, selection of CFD/CAA and surrogate models, and design of optimization processes. More details on these steps are provided in this section whereas the detailed description of the optimization process along with a sensitivity study can be found in Ref. 14.

3.1. Parametrization of blade geometry

The blade parametric model was established using spline-based arrangements of chord, twist, and sweep distributions along the radius. Furthermore, the model incorporated airfoil cambers, extending its scope to encompass radially varying airfoils.

Chord, twist, and sweep distributions along the radius were described by positions of spline knots, ensuring smooth transitions and offering direct control over values at the root and tip sections. Decisions regarding the number of knots and the extent of their adjustability were arbitrary. Five knots were employed for chord and twist distributions (from 0.2 to 1.0 of the blade span) and three knots for sweep distribution (from 0.8 to 1.0 of the blade span), often with fixed placements along the radius to simplify the optimization process. The near-tip region refinement (i.e., the three knots within 20% of the blade tip) was established to allow more design freedom in the most sensitive part of the blade.

Local airfoil shapes were characterized using two baseline airfoils: one for the root and another for the tip. The blade was segmented into three parts along the radius: the inner segment using the root airfoil, the outer using the tip airfoil, and the transitional section with an interpolated airfoil. This configuration is depicted in Figure *1*, where parameters r0, r1, and r2 defined boundaries for successive segments. Parameters r0 and r2 were constant and set to 0.2R and 0.93R respectively, while parameter r1 was optimized. The airfoils were stacked with a reference point situated at 40% of the chord length along the stacking line, established by the sweep distribution. Notably, the stacking line was confined to the xy-plane, indicating the absence of dihedral.

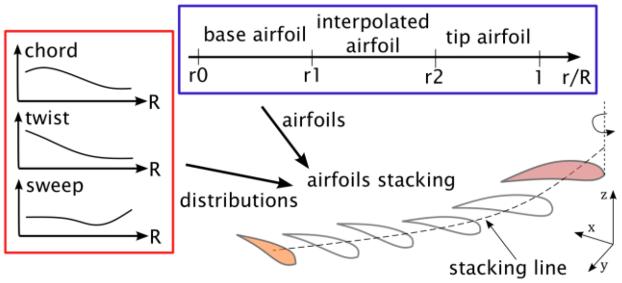

Figure 1: The parametric model of a blade consists of chord, twist and sweep distributions and airfoil shapes.

The objective of airfoil parametrization was to enable significant adjustments to airfoil properties while utilizing as few parameters as possible. Consequently, the parametric model was constructed around a baseline airfoil, allowing modifications to the maximum camber value as well as the chordwise positions of maximum camber and thickness, at the root and tip of the blade independently. By altering these 6 parameters, a relatively expansive design space could be explored. The maximum airfoil thickness was fixed at 10% chord (constant along the blade).

The summary of the parametric model is presented in Figure 1. The total number of 20 parameters described the geometry of the blade.

3.2. CFD model

The aerodynamic model employed in this study relies on high-fidelity RANS simulations. The choice for utilizing a blade-resolved CFD model is driven by two key factors. Firstly, the conditions during hovering involve intricate interactions between the flow around the blade and the wake produced by the preceding blade. These three-dimensional phenomena require appropriate modeling, which rules out the use of cheap blade element-based methods. While comparisons between low-fidelity and high-fidelity models can be carried out (Ref. 15) to identify sources of errors in low-fidelity approaches, the use of high-fidelity simulations is indispensable. Secondly, considering the optimization standpoint, the method must be robust and provide accurate results for various input geometries. Consequently, methods based on two-dimensional airfoil data, which are simplified, can only offer accurate results within a restricted operational range. The proposed model can be also used with more sophisticated parametric models, including geometry features that require blade-resolved CFD, such as winglets.

Finite-volume RANS approach, with eddy-viscosity k−ω SST turbulence model (Ref. 16), was selected for aerodynamics modeling, in a periodic setup. The computational model of a single blade was used, due to the periodic nature of isolated propeller analysis. The computational domain extends 24 radii in the blade direction and 40 radii in the upstream and downstream directions. A single rotating reference frame approach was used to model the propeller rotation. Hover was modeled with pressure–outlet boundary conditions on the non-periodic boundaries of the domain. The setup is presented schematically in Figure 2.

A compressible, coupled pressure-based solver was used with the second order pressure interpolation scheme. The second order-upwind scheme was used for spatial discretization of convection terms. The under-relaxation was controlled by a pseudo-transient approach. With a solution typically converging after around 2000 iterations, an additional 1000 iterations were added to allow for the averaging of a statistically steady solution.

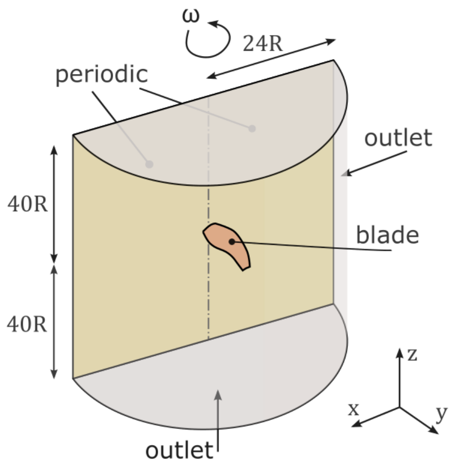

Figure 2: Computational domain setup using boundary conditions.

An unstructured, polyhedral meshing procedure was established to provide case-independent quality of solutions. The near-wall prism thickness was established to ensure y+ in the viscous sub-layer regime, i.e., y+ ≤ 5, while the number of layers was dictated by the need for a smooth transition to unstructured polyhedral. The growth ratio was fixed at 1.18. The resulting area-weighted average of y+ was around a unity with 24 prism layers. The final volume mesh size was between 3.5 to 4 million elements (the number of elements is case-dependent). The example surface mesh on the blade surface is presented in Figure 3.

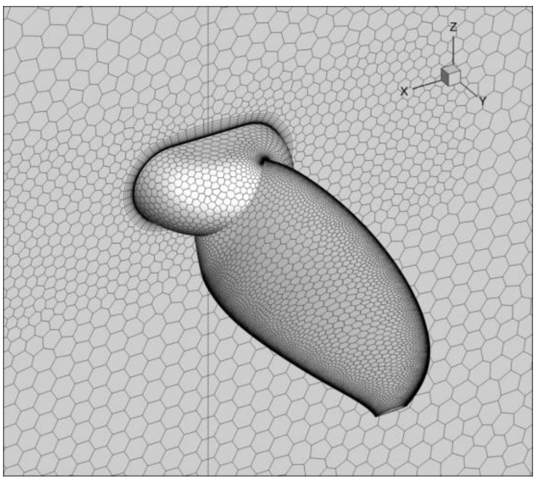

Figure 3: Mesh sizing on blade, hub and periodic surfaces.

Both meshing and CFD were performed using commercial software Ansys Fluent 21.1. The computational time of a single case (meshing and CFD) was between 5 to 6 h using 24 processes.

3.3. CAA model

The pressure signal required to obtain the OASPL at a selected observer location was calculated using the Farassat 1A formulation (F1A) (Ref. 17) of FWH acoustic analogy (Ref. 18), based on the solution of the RANS CFD model. In this approach, the blade is rotated virtually and the pressure distribution on the blade surface is constant. Only tonal noise is captured with this approach, as there are no pressure oscillations resulting from turbulence. Ansys Fluent was used to calculate acoustic signals using the retarded time approach. To ensure sufficient sampling for the tonal noise calculation, acoustic signal was collected 40 times per revolution for 30 revolutions.

3.4. Optimization process

The created optimization environment was developed with general multi-objective and multi-point optimization capabilities in mind. Consequently, a surrogate-based optimization strategy was devised to efficiently establish a Pareto front of propeller geometries in aeroacoustic optimization. Kriging surrogate models (Ref. 19) of thrust, Figure of Merit (FM) and overall sound pressure level (OASPL) were created to perform optimization, with an evolution algorithm used to search the surrogate model for non-dominated solutions.

In the current work, global optimization is considered, with continuous design variables. The cost of a single evaluation of the objective function is sufficiently high to rule out classic global optimization methods, such as direct optimization driven by an evolutionary algorithm. On the other hand, the potential complexity (multimodality) of the search space rules out the use of local optimizers, which are likely to get stuck in a local minimum.

The use of surrogate modeling-driven optimization allows the use of global search methods, which use cheap surrogate prediction. A general procedure for SBO, presented schematically in Figure 4, is:

1. Define an initial sample of points in the search space. Evaluate both aerodynamic

and aeroacoustic metrics of the initial sample based on a CFD/CAA model.

2. Train a surrogate model with the available data (the initial sample and infill points). Assess surrogate model quality (e.g., by cross validation).
3. Find candidate point(s) for verification. The selection of candidates is typically performed by exploration and exploitation of the search space using global search methods.
4. Verify candidate(s). Check process convergence/termination criteria - if not reached go back to step 2.

The initial sample required for a high-quality surrogate model requires a uniform spread of candidate points in the search space. In the current work, the Latin hypercube approach was used (Ref. 20), along with the optimal space-filling criterion (Ref. 21). The surrogate modeling methods and infill criteria used in the current work are based on kriging and follow from the efficiency of Efficient Global Optimization (Ref. 22).

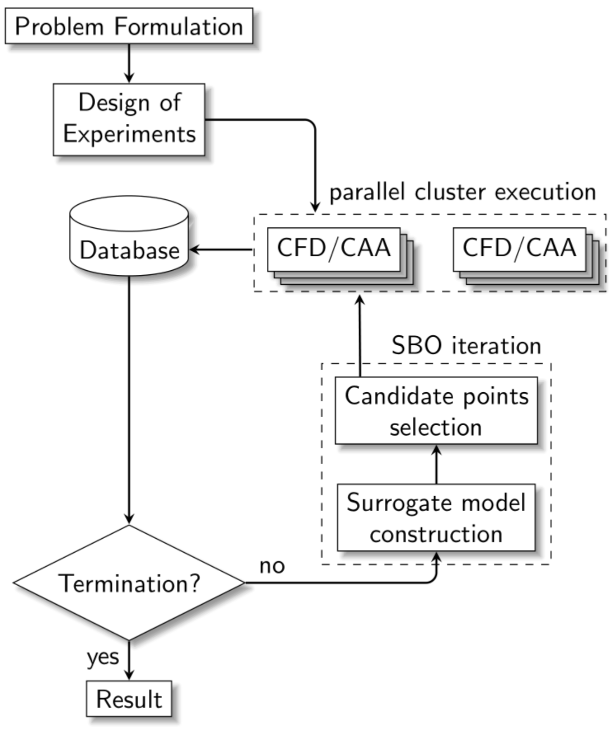

Figure 4: Aeroacoustic surrogate-based optimization framework.

4. EXPERIMENTAL SETUP

The baseline benchmark propeller, as well as three optimized geometries, were tested in the newly-built anechoic chamber at Lukasiewicz Research Network – Institute of Aviation (ILOT). The aerodynamic performance of the rotors was assessed on a custom testing rig, and their acoustic characteristics were determined using a set of free-field microphones. More details on the experimental setup are provided in this section.

4.1. Anechoic chamber

The anechoic chamber at the ILOT is in the form of a freestanding room constructed within an existing hall using a semi-custom drywall system, which rests on an array of mechanical vibration isolators. Internally, the chamber is 4.40 m deep, 4.15 m wide, and 5.00 m high. In order to ensure anechoic conditions within the room, the entire surfaces of the walls, the roof and the floor were covered with foam wedges, with corners filled with appropriate rectangular blocks, leaving no hard surface exposed. The wedges have a total height of 500 mm and a base of 300 × 300 mm with a thickness of 100 mm. The tip-to-tip dimensions of the chamber are 3.40 × 3.15 × 4.00 m. In accordance with the requirements of the ISO 3745 norm, the chamber guarantees anechoic conditions for frequencies above 150 Hz. The background noise inside the chamber does not exceed 17 dB(A).

4.2. Propeller test rig

The propeller testing rig performs two main functions. Firstly, it enables both acoustic and aerodynamic measurements by rotating the propeller at the desired rotational speed. Secondly, it measures the aerodynamic loads exerted by the propeller: the thrust and torque.

To minimize the impact of the testing rig on the aeroacoustic performance of propellers, all the necessary components are contained within a tube with a consistent diameter of 50 mm. This tube, along with the propeller axis, is positioned vertically to guide the propeller wake along the longest dimension of the chamber. The length of the tube is configured so that the propellers are situated approximately 1.3 m above the tips of the floor wedges. Propellers are tested in an inverted orientation. As a result, the propellers generate downward thrust while directing airflow upwards. The fully assembled rig, prepared for tests in the anechoic chamber, is shown in Figure 5.

Embedded within the rig are an AXI 2814/28 V2 BLDC electric motor with a RiKO PRC-630 optical revolution sensor, a FUTEK QTA143 torque meter, and an Octogon FSA-20 thrust meter. The motor is mounted directly to the torque meter, but due to the thrust sensor's fragility (a single M3 interface on both sides), linear bearings were located between the two sensors. These remove lateral loads from the thrust meter.

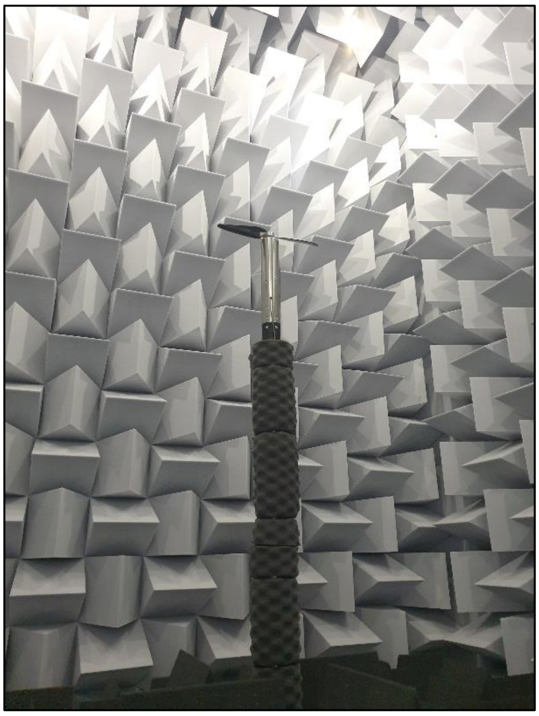

Figure 5: Propeller test rig in the anechoic chamber.

4.3. Data acquisition system

All acoustic measurements were performed using PCB 378B02 free-field microphones. The data acquisition system consisted of two NI cDAQ-9189 chassis with NI-9250 cards for the microphones, as well as NI-9203 and NI-9205 cards for load, RPM and atmospheric sensors. Microphone signals were acquired at 51.2 kHz. Thrust and torque, as well as RPM and the atmospheric parameters, were acquired at 10 kHz. The signals were sampled for 5 s, shortly after the propeller reaches desired rotational speed, to avoid recirculation effects, as discussed in Ref. 23. In the specific experimental configuration, these effects typically begin to manifest approximately 15 seconds after the propeller starts spinning.

The microphones were mounted vertically in a straight line, facing the propeller axis, with the sensing elements 1.2 m away from the axis. The central microphone was mounted in the plane of the propeller, with subsequent microphones 30 cm, 60 cm and 90 cm above and below the in-plane microphone. These positions correspond to the positions used in the benchmark study described in Ref. 24 (every second microphone position was used). However, this paper focuses only on the analysis of acoustic results in the plane of the rotor.

4.4. Propeller prototypes

Propeller prototypes utilized in the experimental study were constructed from aluminum alloy and produced through 5-axis simultaneous CNC milling. This manufacturing method was selected for its capacity to precisely replicate the geometry and provide substantial model rigidity, thereby ensuring minimal elastic deformations during operation. The benchmark propeller was also manufactured using this same process, given that the CAD model for the propeller was provided by the authors of Ref. 24. Examples of the CNC-milled propeller prototypes are illustrated in Figure 6.

Figure 6: CNC-milled propellers.

5. RESULTS

5.1. Benchmark case

In the first step, the computational models were compared and validated against the experimental benchmark from the literature, which was also treated as a baseline case for the presented optimization process.

The benchmark used in this study was published by researchers from the Delft University of Technology (TU Delft) (Ref. 24). A two-bladed propeller was used, derived from a commercial APC 9x6 model, scaled to a 30 cm diameter, and with profiles reshaped using the NACA4412 airfoil. The propeller was machined out of aluminum and was rotated at 5000 RPM in the hover condition and at several advance ratios. Noise characteristics were determined using a column of microphones, as described in section 4.3. Thrust and torque were measured using dedicated sensors, to calculate thrust (C_T) and torque (C_Q) coefficients.

The comparison of the results was prepared only for the hover conditions, focusing on the microphone lying in the plane of the propeller rotation. All cases correspond to 5000 RPM of rotational speed. The most important data was gathered in Table 1.

Table 1: Comparison of experimental and computational data for the benchmark case (Ref. 24).

Characteristic	Exp. (TU Delft)	Exp. (ILOT)	CFD/CAA
T [N]	7.72	8.37	8.11
C_T [-]	0.0150	0.0164	0.0158
C_Q [-]	0.00195	0.00208	0.00224
SPL_{BPF} [dB]	69.67	69.64	68.68
$OASPL$ [dB]	71.02	70.09	68.82
$OASPL$ [dB(A)]	65.41	61.04	56.02

When compared to TU Delft experimental data, it can be seen that the thrust coefficient was overshot by approximately 9.3% in the case of the ILOT experiment and 5.3% in the case of CFD prediction. At the same time, the torque coefficient was overestimated by 6.6% in the ILOT experiment and almost 15% in CFD. A major drawback of the current computational model is the assumption of a fully turbulent flow and the significant differences in torque prediction can be partly attributed to this simplification, especially when compared to experimental results obtained with very smooth propeller blades surfaces. Similar results were obtained using a high-fidelity Lattice-Boltzmann Method in the literature benchmark. Interestingly, both experimental and computational data obtained at ILOT are characterized by higher values of thrust coefficient. The reason for this difference is unknown.

When it comes to acoustic data, three different parameters were calculated: SPL at Blade Passing Frequency (BPF) and overall SPL (OASPL) with and without the A-weighting function applied (according to international standard IEC 61672:2003). Exceptionally good agreement was observed between experiments in the values of SPL at BPF tone. Also in the case of CFD/CAA, the difference is only about 1 dB, which should be considered accurate. The larger discrepancies appear for OASPL values, where the highest values can be seen in the experiment performed at TU Delft, and the lowest in CFD/CAA data. The latter is in line with expectations, as the computational models used can provide information only in terms of tonal noise generated by the propeller. Therefore, the OASPL value for CFD/CAA calculations is very close to SPL_{BPF} (BPF tone is dominant).

The investigation of differences between the OASPL values obtained in both experiments could be done based on the analysis of the noise spectrum, presented in Figure 7 using third-octave SPL. It is clearly seen that the broadband noise levels in the TU Delft experiment are higher than in the ILOT test, especially between 500 and 5000 Hz. This frequency region was said to be significantly affected by motor noise in the benchmark study, and that is also the case in the ILOT measurements. However, the frequency characteristics of the motor noise are different between the two studies, with a narrower frequency range affected in the ILOT data (peak at 1000 Hz), and a much lower noise level between 1500 and 4000 Hz. Taking into account the human perception of noise (using the A-weighting function), the described difference results in a 4.37 dB(A) lower values of OASPL in the ILOT experiment.

Figure 7 includes also a spectrum obtained through CFD/CAA computations and confirms what was stated before about the accurate prediction of only tonal noise components. It should be noted that the $SPL_{1/3}$ values are very accurately reproduced not only near the BPF (about 166 Hz) but also the second harmonic of the BPF (when compared to the ILOT experiment).

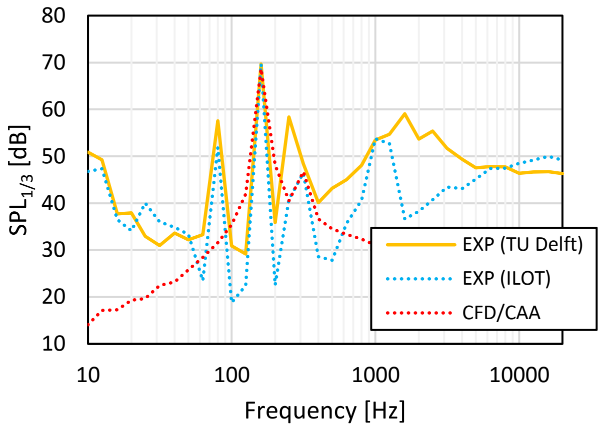

Figure 7: Comparison of the experimental noise spectra with CFD/CAA prediction ($SPL_{1/3}$).

Despite some discrepancies in predicting propeller performance, it should be stated that both experimental and computational approaches seem to agree quite well with benchmark data from TU Delft. Computational models are considered sufficient, especially in the optimization context of the current work, where the ability to predict trends is more important than predicting absolute values.

5.2. Optimization results

Optimization of a 30 cm propeller in hover conditions was performed to demonstrate some of the capabilities of the proposed approach. Based on the initial sample and subsequent infills, surrogate models of selected functions of interest were generated. Then, surrogate-based optima were determined in terms of efficiency (FM) maximization and noise (OASPL) minimization.

The current study was focused on finding the aeroacoustic optima which provide 8 N of thrust in hover. The multi-objective optimization was performed with respect to 20 geometric parameters and rotational speed. The rotational speed was allowed to vary from 4200 to 5000 RPM – it was expected that propellers with lower RPM will have lower noise emission. The target thrust of 8 N was defined as an inequality constraint (introducing tolerance) in order to improve optimization convergence. The expected solution was in the form of a set of non-dominated points forming a Pareto front.

The initial sample was defined using a space-filling algorithm (as stated in section 3.4.) with parameter bounds determined using low-fidelity BET code, to ensure desired propeller properties. The initial sample consists of 200 points, covering a thrust range of 4.5 N to 13 N. The resulting chord and twist distributions of the initial sample are visualized in Figure 8. It can be observed that a large search space was investigated in this study. The need for such variation in blade geometric parameters was dictated by the variable rotational speed, which has a large influence on the resulting forces.

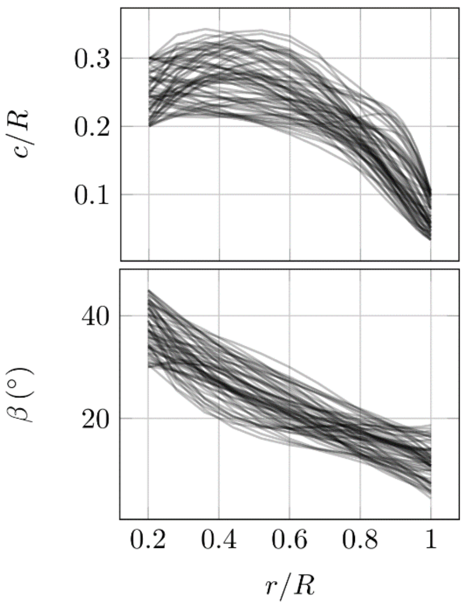

Figure 8: Initial sample chord and twist distributions (every fourth shown for clarity).

The SBO procedure, described in section 3.4, was followed to establish an aeroacoustic Pareto front. The Scipy differential evolution (DE) algorithm (Ref. 25) was used to search for infill points. DE is a stochastic optimization method, used for finding the global optimum of a multivariate function with constraint handling capabilities. The infill criteria used to establish the Pareto set were based on the minimization of OASPL and −FM values.

The iterative optimization procedure was run for 12 infill iterations, improving the surrogate model prediction in the promising areas. This was considered sufficient as no new point was added to the Pareto front for two consecutive iterations. The lack of improvement was attributed to the surrogate prediction error and a very tight margin for potential improvement. The aeroacoustic Pareto front, presented in the bottom-right corner of Figure 9, turned out to be very narrow because individuals with lower OASPL tend to have a higher FM.

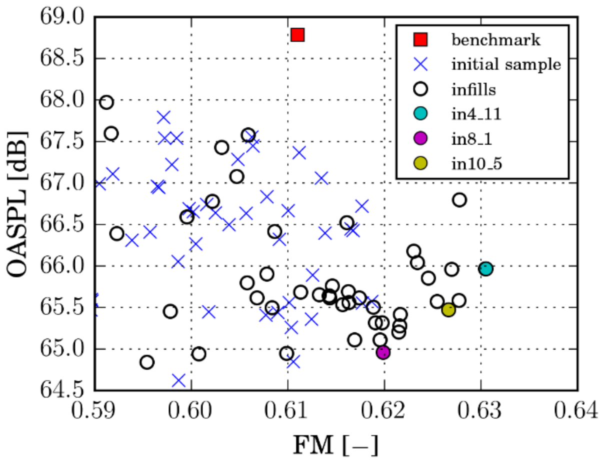

Figure 9: Surrogate-based optimization results (OASPL vs FM; 8N of thrust for all solutions).

The whole optimization process, including both initial sample and infill iterations, took approximately 50–60 thousand CPU hours. Due to parallel case execution, all computations were completed within a week on a high-performance computing cluster. Consequently, SBO applied to RANS-based global propeller design should be considered feasible from a computational point of view.

Figure 10 presents distributions of chord and twist along the radius for two solutions selected from the Pareto front: *in4_11* (FM-optimal) and *in8_1* (OASPL-optimal). Major differences can be observed: the FM optimum has a higher aspect ratio and lower twist, especially in the inboard part of the blade. The design RPM required to achieve the target thrust, is 4740 and 4250 for the FM and OASPL optima, respectively.

The differences in blade geometry translate into changes in their load during operation. The axial and tangential force distributions along the radius, computed from the CFD model, are presented in Figure *11*. It can be seen that the OASPL optimum has the loading shifted towards the rotation axis, compared to the FM optimum. Similarly, peak values are higher for the FM optimum. These trends are expected, as noise reduction is achieved by lowering peak pressure, which is the highest near the tip.

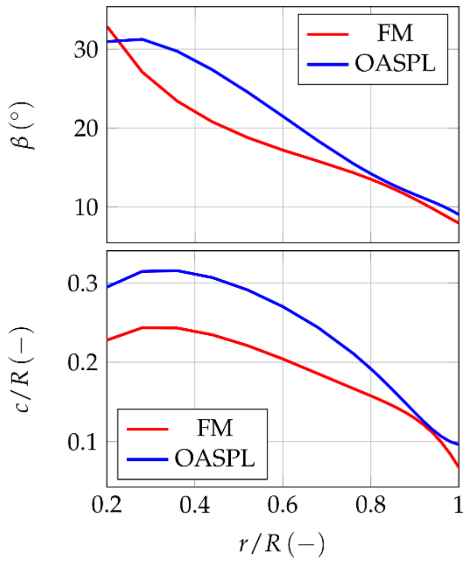

Figure 10: Chord and twist distributions describing the geometries of the FM- and OASPL-optimal designs.

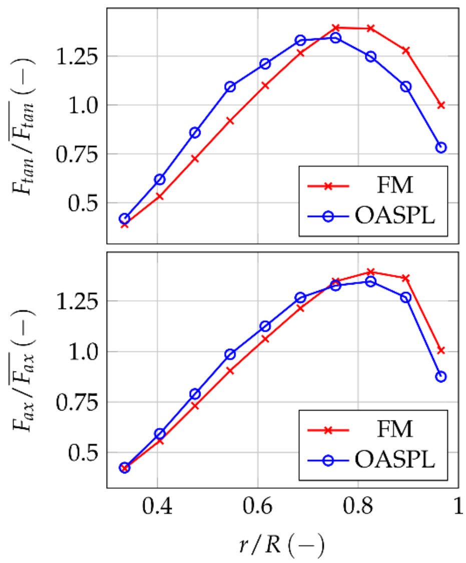

Figure 11: Axial and tangential forces along the radius for FM- and OASPL-optimal designs. Forces are scaled by the average value along the radius.

To conclude the optimization results, it should be noted that all expected trends regarding noise-minimizing propeller design were reproduced. The optimization process allowed for the emergence of solutions with lower noise emissions and better efficiency than the baseline (benchmark) propeller, as shown in Figure 9.

5.3. Validation of design methodology

To validate the results and capabilities of the presented design methodology, three Pareto-optimal geometries were selected for CNC-milling and testing. The final selection was done based on the Pareto front plotted using the A-weighted OASPL value, shown in the bottom-right corner of Figure 12, to account for the relative loudness perceived by the human ear. The solution with the highest attained FM (*in4_11*), and two with lower OASPL values (*in10_5*, *in8_1*) were chosen. In this case, switching to the A-weighted OASPL made it a bit easier to select individuals for manufacturing and testing. It is also worth noting the greater differences between the benchmark and the optimized propellers in terms of noise values in dB(A), resulting from different rotational speeds. The predicted difference between the extreme selected solutions was slightly less than 3 dB(A) and just above 0.01 FM counts.

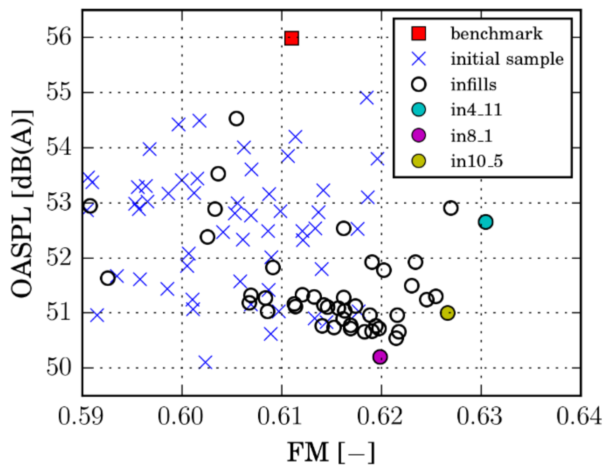

Figure 12: Surrogate-based optimization results (A-weighted OASPL vs FM; 8N of thrust for all solutions).

The performance and acoustics of the manufactured propellers were verified on the test stand within the ILOT anechoic chamber, both described in section 4. Each propeller was tested at a rotational speed that guarantees the same amount of thrust (8 N). All propellers were tested in similar atmospheric conditions – the range of air density variation during tests was 1.163-1.171 kg/m^3.

Table 2 summarizes the most important results of experimental tests concerning both the propeller efficiency in hover and the generated noise. For the optimized propellers, the absolute values of measured parameters and the differences in relation to the values measured for the benchmark are given.

Table 2: Summary of experimental studies - comparison of propeller performance and acoustics at 8N thrust.

Propeller	FM [-]	$OASPL$ [dB(A)]	SPL_{BPF} [dB(A)]
benchmark	0.719	61.78	56.19
in4_11	0.742 (+0.023)	60.61 (-1.17)	53.25 (-2.94)
in8_1	0.689 (-0.030)	57.36 (-4.43)	49.98 (-6.21)
in10_5	0.690 (-0.029)	56.36 (-5.43)	51.02 (-5.17)

Analyzing the values of the FM parameter, it can be seen that not all optimized propellers showed a performance improvement compared to the benchmark. In the case of the *in4_11* propeller, the predicted and measured change in the FM parameter value is very similar (about +0.02). For the remaining propellers, the agreement of the experimental results with the surrogate predictions is much worse, even when taking into account the differences, not absolute values. The discrepancies in absolute values, approx. 0.1 for the benchmark, are probably due to the assumptions of the CFD model, discussed in section 5.1. The propellers for which the greatest errors in FM values are observed (*in10_5*, *in8_1*) are characterized by a lower rotational speed (approx. 4200 RPM) and larger angles of attack. In combination with the low Reynolds number flows, this is a great challenge for the computational model, and thus is the probable cause of the discrepancies obtained.

In the field of acoustics, the focus was on the parameters corrected using the A-weighting function. The OASPL value reflecting the overall noise level of the propeller may seem like the most important parameter. All optimized propellers turned out to be quieter than the benchmark, but the improvements are not perfectly consistent with the prediction shown in Figure 12. In the case of the *in4_11* prototype, the reduction of OASPL is only 1.17 dB(A), while the predicted value is about 3.3 dB(A). The quietest propeller, as predicted by the surrogate, should be *in8_1*, while in the experiment the lowest OASPL value was obtained with *in10_5*. However, when comparing the values of the experimentally measured OASPL parameter (especially the A-weighted parameter), the issues mentioned in section 5.1 should be borne in mind. Firstly, the presence of other noise sources (motor noise) may affect the OASPL value differently for different cases, making it difficult to compare propellers. Secondly, possible changes in the broadband noise generated by the propellers, also affecting the OASPL values, could not be captured by the computational models used. Therefore, using the OASPL value to validate the optimization results is not entirely representative.

Noticeably better agreement between optimization and experiment results was obtained by analyzing the SPL value at BPF, taking into account only the tonal noise generated by the propeller. When compared to the OASPL obtained numerically, it can be seen that a very good quantitative agreement was achieved, even for absolute noise values. The successful prediction and minimization of tonal noise for optimized propellers should be considered a very useful feature of the proposed design methodology, as this noise component is of particular importance for noise perception and human well-being.

6. CONCLUSIONS

Capabilities of a methodology for designing rotors with low noise emission and high performance were demonstrated through exemplary UAV propeller multi-objective optimization. Three Pareto-optimal geometries and the benchmark propeller were CNC-milled to perform tests on a dedicated test stand in an anechoic chamber, and to validate computational tools and optimization results.

The most important conclusions of the work are:

1. The developed optimization framework proved to be able to provide solutions for the aeroacoustics optimization of UAV propeller, with the highly capable blade-resolved RANS computational model employed and at acceptable computational cost, due to a surrogate-based approach. The surrogate-based non-dominated solutions were improved relative to the benchmark baseline, both in terms of aerodynamic performance and noise level.

2. Based on the benchmark case, it was proven that the developed acoustic facility at ILOT (anechoic chamber and test rig) is able to provide high-quality propeller acoustic and performance data and could be used to validate the proposed design methodology. By comparing with data from TU Delft, the need to eliminate unwanted noise sources during the tests was highlighted, as they might significantly affect e.g. the propeller OASPL values.

3. The observed direction of optimization and the properties of the obtained geometries are in line with the expectations and trends reported in the literature.

4. Validation of the optimization results showed a very good agreement between the experimentally obtained tonal noise characteristics and those predicted by the CFD/CAA-based surrogate model. Slightly different conclusions from the analysis of the A-weighted OASPL values may suggest a non-negligible effect of broadband noise contribution at the analyzed scale of propellers.

5. Validation of the optimization results revealed discrepancies in the predicted and measured performance trends between manufactured prototypes, especially visible for the low-RPM propellers. This was attributed to the limitations of the CFD model related to the low Reynolds number and high angle of attack flows.

The presented optimization case concerned only hover conditions, but it is not a limitation of the developed framework, capable of multi-point design. More complex cases, including e.g. cruise conditions, will be analyzed in the future. This paper focuses solely on the tonal component of noise. Accounting for broadband noise is another area for method development, especially important for small-scale UAV rotors.

Author contact:

Adam Sieradzki
adam.sieradzki@ilot.lukasiewicz.gov.pl

Pawel Kekus
pawel.kekus-kumor@ilot.lukasiewicz.gov.pl

Witold Klimczyk
witold.klimczyk@ilot.lukasiewicz.gov.pl

7. ACKNOWLEDGMENTS

The authors would like to thank Edoardo Grande and Daniele Ragni from TU Delft for providing additional benchmark data, as well as Paweł Kmita and Maciej Osiewicz from ILOT for their work on the propeller testing rig. Computations were carried out using the computers of Centre of Informatics Tricity Academic Supercomputer & Network.

8. REFERENCES

1. S. A. Rizzi, D. L. Huff, D. D. Boyd, P. Bent, B. S. Henderson, K. A. Pascioni, D. C. Sargent, D. L. Josephson, M. Marsan, H. He, and R. Snider, 'Urban Air Mobility Noise: Current Practice, Gaps, and Recommendations', NASA, NASA/TP-2020-5007433, Oct. 2020.

2. O. Barbara, L. Seth, A. Roalt, D. Schreckenberg, and M. V. Miltenburg, 'Association Between Short-Term Annoyance and Several Physiological Parameters During Different Amounts of Nocturnal Aircraft Noise Exposure', *Transactions on Aerospace Research*, vol. 2020, no. 4, pp. 1–12, Dec. 2020, doi: 10.2478/tar-2020-0018.

3. A. W. Christian and R. Cabell, 'Initial Investigation into the Psychoacoustic Properties of Small Unmanned Aerial System Noise', in *23rd AIAA/CEAS Aeroacoustics Conference*, in AIAA AVIATION Forum. American Institute of Aeronautics and Astronautics, 2017. doi: 10.2514/6.2017-4051.

4. W. A. Klimczyk, 'Aerodynamic design and optimization of propellers for multirotor', *Aircraft Engineering and Aerospace Technology*, vol. 94, no. 1, pp. 21–30, Jan. 2022, doi: 10.1108/AEAT-12-2020-0288.

5. D. Ingraham, J. S. Gray, and L. V. Lopes, 'Gradient-Based Propeller Optimization with Acoustic Constraints', in *AIAA Scitech 2019 Forum*, San Diego, California: American Institute of Aeronautics and Astronautics, Jan. 2019. doi: 10.2514/6.2019-1219.

6. R. Serré, H. Fournier, and J.-M. Moschetta, 'A design methodology for quiet and long endurance MAV rotors', *International Journal of Micro Air Vehicles*, vol. 11, Jan. 2019, doi: 10.1177/1756829319845937.

7. O. Gur, J. Silver, R. Dítě, and R. Sundhar, 'Optimized Performance and Acoustic Design for Hover-Propeller', in *AIAA AVIATION 2021 FORUM*, Virtual Event: American Institute of Aeronautics and Astronautics, Aug. 2021. doi: 10.2514/6.2021-2222.

8. N. S. Zawodny, D. D. Boyd, and C. L. Burley, 'Acoustic Characterization and Prediction of Representative, Small-Scale Rotary-Wing Unmanned Aircraft System Components', presented at the American Helicopter Society (AHS) Annual Forum, West Palm Beach, FL, May 2016. Accessed: Aug. 08, 2023. [Online]. Available: https://ntrs.nasa.gov/citations/20160009054

9. T. F. Brooks, D. S. Pope, and M. A. Marcolini, 'Airfoil self-noise and prediction', NASA Langley Research Center, Hampton, VA, USA, Jul. 1989. Accessed: Aug. 11, 2023. [Online]. Available: https://ntrs.nasa.gov/citations/19890016302

10. F. R. Menter, 'Best Practice: Scale-Resolving Simulations in Ansys CFD', ANSYS, Inc., Canonsburg, PA, USA, 2015. [Online]. Available: https://www.ansys.com/content/dam/product/fluids/cfd/tb-best-practices-scale-resolving-models.pdf

11. G. Romani, E. Grande, F. Avallone, D. Ragni, and D. Casalino, 'Performance and noise prediction of low-Reynolds number propellers using the Lattice-Boltzmann method', *Aerospace Science and Technology*, vol. 125, Jun. 2022, doi: 10.1016/j.ast.2021.107086.

12. L. Wang, B. Diskin, L. V. Lopes, E. J. Nielsen, E. Lee-Rausch, and R. T. Biedron, 'High-Fidelity AeroAcoustic Optimization Tool for Flexible Rotors', *Journal of the American Helicopter Society*, 2020, doi: 10.4050/JAHS.66.022004.

13. B. Marinus, M. Roger, and R. Van Den Braembussche, 'Aeroacoustic and Aerodynamic Optimization of Aircraft Propeller Blades', in *16th AIAA/CEAS Aeroacoustics Conference*, Stockholm, Sweden: American Institute of Aeronautics and Astronautics, Jun. 2010. doi: 10.2514/6.2010-3850.

14. W. Klimczyk and A. Sieradzki, 'RANS-Based Aeroacoustic Global Sensitivity Study and Optimization of UAV Propellers', *Aerospace*, vol. 10, no. 3, Mar. 2023, doi: 10.3390/aerospace10030306.

15. N. Mourousias, A. Malim, B. G. Marinus, and M. Runacres, 'Surrogate-Based Optimization of a High-Altitude Propeller', in *AIAA AVIATION 2021 FORUM*, in AIAA AVIATION Forum. American Institute of Aeronautics and Astronautics, 2021. doi: 10.2514/6.2021-2597.

16. F. R. Menter, 'Two-equation eddy-viscosity turbulence models for engineering applications', *AIAA Journal*, vol. 32, no. 8, pp. 1598–1605, Aug. 1994, doi: 10.2514/3.12149.

17. K. S. Brentner and F. Farassat, 'Modeling aerodynamically generated sound of helicopter rotors', *Progress in Aerospace Sciences*, vol. 39, no. 2–3, pp. 83–120, Feb. 2003, doi: 10.1016/S0376-0421(02)00068-4.

18. J. E. F. Ffowcs-Williams and D. L. Hawkings, 'Sound Generation by Turbulence and Surfaces in Arbitrary Motion', *Philosophical Transactions of the Royal Society of London. Series A, Mathematical and Physical Sciences*, vol. 264, no. 1151, pp. 321–342, 1969.

19. D. R. Jones, 'A taxonomy of global optimization methods based on response surfaces', *Journal of global optimization*, vol. 21, no. 4, pp. 345–383, 2001.

20. A. I. J. Forrester and A. J. Keane, 'Recent advances in surrogate-based optimization', *Progress in Aerospace Sciences*, vol. 45, no. 1–3, pp. 50–79, Jan. 2009, doi: 10.1016/j.paerosci.2008.11.001.

21. M. D. Morris and T. J. Mitchell, 'Exploratory designs for computational experiments', *Journal of Statistical Planning and Inference*, vol. 43, no. 3, pp. 381–402, Feb. 1995, doi: 10.1016/0378-3758(94)00035-T.

22. D. R. Jones, M. Schonlau, and W. J. Welch, 'Efficient Global Optimization of Expensive Black-Box Functions', *Journal of Global Optimization*, vol. 13, no. 4, pp. 455–492, Dec. 1998, doi: 10.1023/A:1008306431147.

23. D. Weitsman, J. H. Stephenson, and N. S. Zawodny, 'Effects of flow recirculation on acoustic and dynamic measurements of rotary-wing systems operating in closed anechoic chambers', *The Journal of the Acoustical Society of America*, vol. 148, no. 3, pp. 1325–1336, Sep. 2020, doi: 10.1121/10.0001901.

24. D. Casalino, E. Grande, G. Romani, D. Ragni, and F. Avallone, 'Definition of a benchmark for low Reynolds number propeller aeroacoustics', *Aerospace Science and Technology*, vol. 113, Jun. 2021, doi: 10.1016/j.ast.2021.106707.

25. P. Virtanen *et al.*, 'SciPy 1.0: fundamental algorithms for scientific computing in Python', *Nat Methods*, vol. 17, no. 3, Mar. 2020, doi: 10.1038/s41592-019-0686-2.

9. CLASSIFICATION & COPYRIGHT